



# Properties of sol gel synthesized ZnO nanoparticles

B. Manikandan<sup>1</sup> · Tamio Endo<sup>2</sup> · Satoru Kaneko<sup>3</sup> · K. R. Murali<sup>4</sup> · Rita John<sup>1</sup> 

Received: 12 December 2017 / Accepted: 21 March 2018 / Published online: 3 April 2018  
© Springer Science+Business Media, LLC, part of Springer Nature 2018

## Abstract

In this work, zinc oxide (ZnO) nanoparticles were synthesized by the sol gel method using zinc acetate as precursor. The synthesized powder was characterized by X-ray diffraction, Fourier transform infrared Spectroscopy (FTIR), Raman, UV–Visible spectroscopy, field emission scanning electron microscopy (FE-SEM), energy dispersive X-ray analysis (EDAX), impedance analysis and photocatalysis activity studies. X-ray diffraction studies indicate that ZnO nanoparticles have single phase with wurtzite hexagonal structure. The lattice parameters were estimated using Scherrer formula. Micro strain, stress, energy density and crystallite size were analysed using Williamson–Hall model. The FTIR spectrum showed the characteristic absorption peak of ZnO at  $458.82\text{ cm}^{-1}$  and authenticates the presence of ZnO nanoparticles. The FE-SEM characterization shows flake like morphology and the presence of chemical element composition is identified in the EDAX analysis. The optical band gap was found to be 3.1 eV. The presence of Zn–O stretching mode was confirmed from Raman spectrum. The electrical properties such as dielectric constant, dielectric loss, and ac conductivity were analyzed from impedance data. The prepared ZnO nanoparticles show good photocatalytic behaviour for methylene blue dye and the rate constant was calculated as  $0.0296\text{ min}^{-1}$ .

## 1 Introduction

Zinc oxide is a material of great interest due to its low cost, availability, and non-toxicity. In the last few decades, ZnO plays an inevitable role among researchers due to its physical, chemical, and optoelectronic properties such as, wide bandgap, good optical transparency, high electron mobility, and photostability [1–3]. These properties are found to be important for various applications such as photocatalysis, solar cells, sensors, and in the field of medicine as well. The particle size and morphology are very important for various applications and in this respect, many research groups are widely involved in the investigation of ZnO nanomaterials [2–5]. ZnO nanoparticles were synthesized by various

well-known techniques, such as co-precipitation method, hydrothermal method, microemulsion, chemical bath deposition, sol–gel, and spray pyrolysis methods [2–6]. Among these, sol–gel method is the simplest route to synthesize nano scale materials as it has the merits of homogeneity and control over temperature. Hence in the present work, the sol–gel method was employed to synthesize ZnO nanoparticles by controlling pH using sodium hydroxide (NaOH).

The addition of NaOH is playing an important role during synthesis process; in sol gel method the role of NaOH is to control the crystallite size and shape [7, 8]. The aim of the present work is to synthesize ZnO nanoflakes using sol gel process to be used as a photocatalyst. The structural, electrical and optical properties of the ZnO nanoflakes are studied using various characterization techniques: X-ray diffraction, FTIR-spectrum, Raman, UV–Vis, FE-SEM, EDAX and Impedance analysis. Two main parameters that can be calculated from the XRD peak width are crystallite size and lattice strain. Lattice strain is due to imperfections such as lattice dislocation and grain boundary. The above-mentioned properties have effective impact on intensity, peak width, and shift in the Bragg's angle [9, 10]. The relationship between lattice strain with crystallite size, stress, energy density, and volume average were investigated through Williamson–Hall model, such as Uniform Deformation Model

✉ Rita John  
ritajohn.r@gmail.com

<sup>1</sup> Department of Theoretical Physics, University of Madras, Chennai, India

<sup>2</sup> Sagamihara Surface Laboratory, Sagamihara, Kanagawa, Japan

<sup>3</sup> Kanagawa Institute of Industrial Science and Technology, Ebina, Kanagawa, Japan

<sup>4</sup> Electrochemical Material Science Division, CSIR- Central Electrochemical Research Institute, Karaikudi, India

(UDM), Uniform Stress Deformation Model (USDM), Uniform Deformation Energy Density Model (UDEDM), and Size-Strain Plot (SSP). In addition to this, photocatalytic degradation of methylene blue (MB) dye was studied. The degradation profile of methylene blue in the presence of ZnO nanoflakes provides excellent photocatalytic activity. This is because of increased interfacial interaction between the ZnO nanoflakes and the dye molecules.

## 2 Experimental details

### 2.1 Materials

Zinc acetate ( $C_4H_6O_4Zn \cdot 2H_2O$ , 99.5% Purity), Ethanol (99.9% purity) and Sodium Hydroxide (NaOH, 98% purity).

### 2.2 Preparation

50 ml of ethanol was added to 4.4 g of zinc acetate and stirred for 1 h with a magnetic stirrer. The pH value of the solution was measured to be around 3. NaOH was added to the above solution drop by drop to increase the pH value to 8. The sol solution was again stirred for 3 h to get the homogeneous gel. The temperature was maintained at 60 °C throughout the synthesis. The gel was further kept to age overnight and washed several times with ethanol as well as distilled water. The obtained gel was dried and ground, powdered with agate mortar. Finally, it was annealed at 500 °C for 4 h.

### 2.3 Characterization techniques

X-ray diffraction (XRD) measurement was performed using powder X-ray diffractometer (SEIFERT JSO2002) equipped with monochromatic  $CuK\alpha_1$  radiation ( $\lambda = 0.154056$  nm). FTIR spectroscopy in the range 400–4000  $cm^{-1}$  was measured by using a Bruker FTIR spectrometer. Raman spectroscopy (Nanophoton Raman-11, Japan) techniques were used for Raman spectrum analysis of ZnO nanoflakes. The absorption spectrum was recorded using UV-Vis-NIR spectrometer (Varian, model 500). The field emission scanning electron microscopy (FESEM) and energy dispersive X-ray spectroscopy (EDAX) were carried out using HITACHI SU6600. The electrochemical impedance (EIS) spectral experiment was performed using computer-controlled Hewlett-packard (model HP428A) electrochemical instrument.

### 2.4 Photocatalytic degradation

Degradation of Methylene blue (MB) dye, procured from Unilab Asia Pacific Speciality Chemicals Limited was used to study the photocatalytic activities of the ZnO nanoflakes

synthesized as described above. The photocatalytic reaction was conducted at room temperature by illuminating the reaction beaker (Pyrex) from a distance of 6 cm with Philips UV light  $2 \times 15$  W UV tube (365 nm). For the reaction, 20 mg of ZnO catalyst was dispersed in 100 ml of methylene blue aqueous solution. The pH of the solution was constant at 10 throughout the experiment. The solution mixture was stirred continuously at a stirring rate of 1000 rpm in order to eliminate the external mass transfer effect. Before irradiating the solution mixture, the suspension was stirred at the rate of 800 rpm in dark for 30 min to establish the adsorption/desorption equilibrium of methylene blue. 5 ml sample was withdrawn every 30 min. The aqueous samples were centrifuged to remove any suspended solid catalyst particles. The residual concentration of methylene blue was measured at 665 nm using the UV-Vis spectrophotometer (Perkin-Elmer with  $\lambda = 650$  nm) in liquid cuvette configuration with de-ionized water as reference.

## 3 Results and discussion

### 3.1 X-ray diffraction analysis

The X-ray diffraction peaks of ZnO nanoflakes are shown in Fig. 1. The peaks at 31.77 (100), 34.49 (002), 36.24 (101), 47.58 (102), 56.52 (110), 62.91 (103), 68.08 (112), and 69.14 (201) clearly show the presence of hexagonal wurtzite ZnO

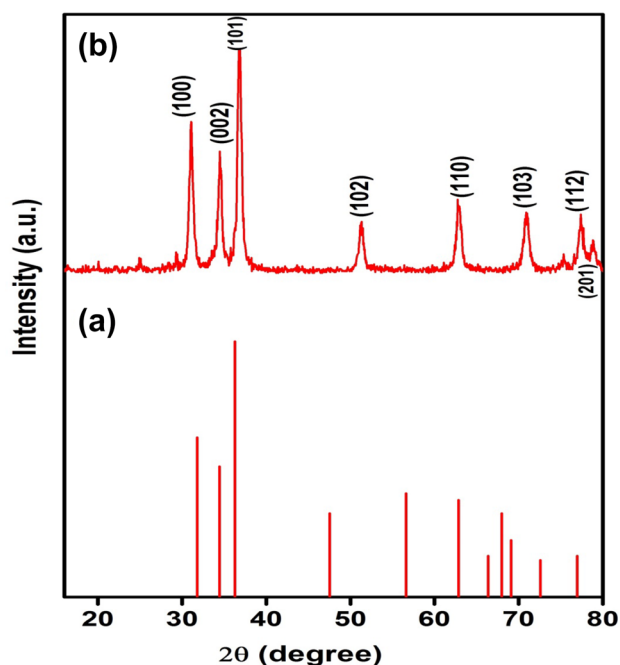


**Fig. 1** The XRD pattern of ZnO nanoflakes, **a** standard XRD pattern of hexagonal ZnO (JCPDS File # 36-1451) and **b** the XRD pattern of ZnO synthesized in the present study

structure. The maximum intensity peak at  $2\theta = 36.24^\circ$  was obtained with (101) orientation. The obtained peak values are well matched with JCPDS File # 36-1451 [11]. The sharpness in the peak endorses that the synthesized material is crystalline. The lattice constants  $a$ ,  $c$ , interplanar spacing ( $d$ ), unit cell volume ( $V$ ), and Zn–O bond length were calculated by using the following formulae. The wavelength of  $\text{CuK}\alpha_1$  ( $\lambda = 0.154056$  nm) was used to calculate the lattice parameters [12];

$$a = \frac{\lambda}{\sqrt{3}\sin\theta} \quad (1)$$

$$c = \frac{\lambda}{\sin\theta} \quad (2)$$

$$\frac{1}{d_{(hkl)}^2} = \frac{4}{3} \left( \frac{h^2 + hk + k^2}{a^2} \right) + \frac{l^2}{c^2} \quad (3)$$

$$V = \frac{\sqrt{3}}{2} a^2 c \quad (4)$$

$$L = \sqrt{\frac{a^2}{3} + \left(\frac{1}{2} - u\right)^2} \quad (5)$$

respectively, where ‘ $u$ ’ is the positional parameter in the wurtzite hexagonal structure and it is the amount by which each atom is displaced with respect to the next atom. ‘ $u$ ’ is given by Eq. (6) and the obtained values are tabulated in Table 1.

$$U = \frac{a^2}{3c^2} + 0.25. \quad (6)$$

**Table 1** The calculated structural parameters of ZnO nanoparticles calcined at 500 °C

Parameter	Calculated value
The Bragg's angle ( $2\theta$ ) for (101) plane (in degree)	36.24
Structure	Wurtzite hexagonal
Lattice parameters (Å)	$a = 2.8789$ $c = 4.9848$ $c/a = 1.7315$ $u = 0.3612$
Crystallite size (D)	21.84 nm
Dislocation density ( $\delta$ )	$2.0964 \times 10^{-3} \text{ (nm)}^{-2}$
Inter planar spacing ( $d_{hkl}$ ) in (Å)	2.2299
Unit cell volume in (Å) <sup>3</sup>	35.78
Strain	$0.951 \times 10^{-3}$

## 3.2 Crystallite size analysis

### 3.2.1 Scherrer method

The crystallite size and lattice strain due to dislocation density can be determined from XRD data. The crystallite size and the dislocation density ( $\delta$ ) of the ZnO nanoparticles were calculated using Scherrer formula in Eqs. (7) and (7a) respectively. The calculated crystallite size and dislocation density of ZnO nanoparticles are 21.84 nm and  $2.09 \times 10^{-3} \text{ (nm)}^{-2}$  respectively. The obtained dislocation density is in good agreement with the already reported values [13, 14]. The crystallite size is a coherently diffracting domain and it is not the same as the particle size due to the presence of polycrystalline aggregates. The Scherrer formula is given by Eq. (7)

$$D = \frac{K}{\lambda} \beta \cos \theta \quad (7)$$

$$\delta = \frac{1}{D^2}, \quad (7a)$$

where,  $D$  is the Crystallite size in nm scale,  $\delta$  is the Dislocation density,  $K$  is the Shape factor which is equal to 0.94,  $\lambda$  is the the wavelength of X-ray radiation of  $\text{CuK}\alpha_1$  ( $\lambda$  is the 0.154056 nm),  $\beta$  is the the full width half maximum intensity (FWHM),  $\theta$  is the the Bragg angle.

### 3.2.2 Williamson–Hall (W–H) methods

The crystal imperfections and distortions are the reasons for the strain induced line broadening. According to Williamson and Hall, it is due to crystallite size and strain contribution. It is related by the following equation

$$\epsilon = \beta_\epsilon / (4 \tan \theta) \quad (8)$$

From Eqs. (7) and (8), it is understood that crystallite size varies with  $1/\cos\theta$  from Scherrer equation and strain varies with  $1/\tan\theta$  from Williamson–Hall equation. Therefore, the total peak broadening is the sum of the contribution of crystallite size and strain. It can be written as Eq. (9)

$$\beta_{hkl} = \beta + \beta_\epsilon \quad (9)$$

where,  $\beta$  is due to the contribution of crystallite size,  $\beta_\epsilon$  is due to the strain induced broadening, and  $\beta_{hkl}$  is full width half maximum intensity of instrumental corrected broadening. It can be given by the following equation

$$\beta_{hkl} = \left[ (\beta_{hkl})^2_{\text{measured}} - (\beta_{hkl})^2_{\text{instrumental}} \right]^{1/2} \quad (10)$$

If the particle size and stain contribution are considered to be independent of each other, then, line breadth is the sum of Eqs. (7) and (8).

$$\beta_{hkl} = \frac{K}{\lambda} D \cos \theta + 4\epsilon \tan \theta \tag{11}$$

By rearranging

$$\beta_{hkl} \cos \theta = \frac{K}{\lambda} D + 4\epsilon \sin \theta \tag{12}$$

$$Y_{(hkl)} = \frac{\left[ h^2 + \frac{(h+2k)^2}{3} + \left( \frac{al}{c} \right)^2 \right]^2}{\left( S_{11} \left( h^2 + \left\{ \frac{(h+2k)^2}{3} \right\} \right)^2 + S_{33} \left( \frac{al}{c} \right)^4 + (2S_{13} + S_{44}) \left( h^2 + \frac{(h+2k)^2}{3} + \left( \frac{al}{c} \right)^2 \right) \right)} \tag{14}$$

The above Eq. (12) is the Williamson–Hall equation [10, 14, 15]. This equation is also known as the Uniform Deformation Model (UDM). In this model, the crystal is considered to be isotropic in nature and hence, the strain is uniform in all crystallographic directions. In Eq. (12), the values of  $\beta_{hkl} \cos \theta$  and  $4\sin \theta$  are taken along Y and X axis respectively. The ‘Y’ intercept of the linear fit gives the crystallite size and the slope of the linear fit the strain value. The UDM plot is shown in Fig. 2. The assumptions on the homogeneity and isotropic nature are not true in all cases. Consequently, the Williamson–Hall equation is modified with the inclusion of anisotropic strain and is known as the Uniform Stress Deformation Model (USDM). In this model, stress is assumed to be uniform in all crystallographic directions whereas small microstrain exists in the material [13]. This assumption is valid only for small strain. When strain is increased the linear proportionality exists no longer. It is well known that Hooke’s law gives the relation between stress and strain and is given by  $\sigma = \epsilon Y_{hkl}$ , where,

$\sigma$  represents stress,  $\epsilon$  represents anisotropic strain, and  $Y_{hkl}$  represents the modulus of elasticity. This relation is simply approximation and is suitable for small strain. When strain is increased the particles will be deviated from its linearity. In this approach the William hall equation can be modified by substituting  $\epsilon$  value in Eq. (12).

$$\beta_{hkl} \cos \theta = \frac{K\lambda}{D} + \frac{4\sigma \sin \theta}{Y_{hkl}} \tag{13}$$

Young’s modulus for hexagonal structure is given by the following equation.

where,  $S_{11}$ ,  $S_{13}$ ,  $S_{33}$ , and  $S_{44}$  are the elastic compliances of ZnO material [10] and their corresponding values are  $S_{11} = 7.858 \times 10^{-12}$ ,  $S_{13} = -2.206 \times 10^{-12}$ ,  $S_{33} = 6.940 \times 10^{-12}$ , and  $S_{44} = 23.57 \times 10^{-12} \text{ m}^2 \text{ N}^{-1}$  respectively.

$\beta_{hkl} \cos \theta$  is plotted against  $4\sin \theta / Y_{hkl}$  and is shown in Fig. 3. The slope of the linear fit gives the uniform deformation stress and the Y-intercept the crystallite size. When considering the energy density of the crystal, the proportionality constant between stress and strain is no longer independent. This approach is also called the Uniform Deformation Energy Density Model (UDEDM) [13]. In this model, the crystal is assumed to be homogenous and isotropic in nature. The energy density of the crystal can be calculated with the help of Hooke’s relation. The energy density as a function of strain is  $u_{ed} = \frac{\epsilon^2 Y_{hkl}}{2}$ , then the Eq. (13) can be modified with respect to energy and strain relation as.

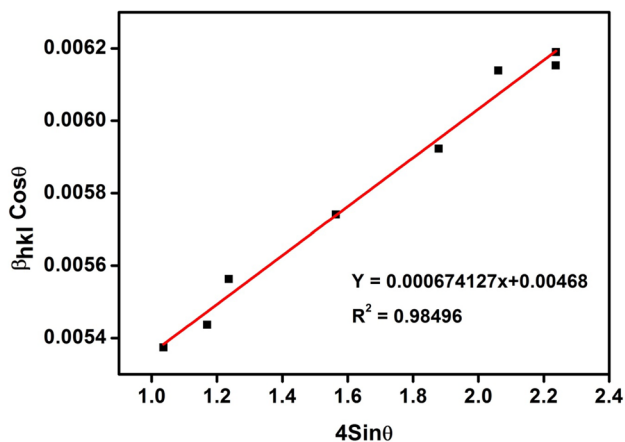


Fig. 2 Plot for  $\beta_{hkl} \cos \theta$  versus  $4\sin \theta$

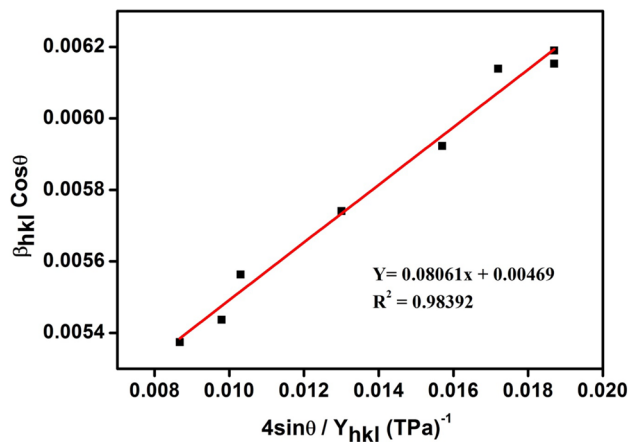


Fig. 3 Plot for  $\beta_{hkl} \cos \theta$  versus  $4\sin \theta / Y_{hkl}$

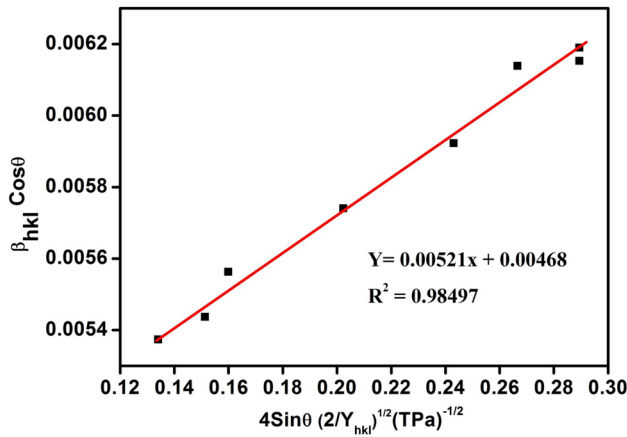


Fig. 4 Plot for  $\beta_{hkl} \cos \theta$  versus  $4 \sin \theta \left( \frac{2}{Y_{hkl}} \right)^{1/2}$

$$\beta_{hkl} \cos \theta = \frac{K\lambda}{D} + 4 \sin \theta \left( \frac{2u_{ed}}{Y_{hkl}} \right)^{1/2} \quad (15)$$

The energy density value can be obtained from the plot between  $\beta_{hkl} \cos \theta$  (X-axis) and  $4 \sin \theta \left( \frac{2u_{ed}}{Y_{hkl}} \right)^{1/2}$  (Y-axis) and is shown in Fig. 4. The slope and Y-intercept gives the anisotropic energy density ( $u_{ed}$ ) and crystallite size ( $D$ ) respectively. The calculated values are consolidated in Table 2.

3.2.3 Size-strain plot method (SSP)

In Williamson–Hall method, it is understood that the line broadening must be isotropic due to the strain contribution [13]. The strain profile is calculated from Gaussian function and crystallite size from Lorentzian function. They are given by Eq. (16).

$$(d_{hkl} \beta_{hkl} \cos \theta_{hkl})^2 = \frac{1}{V_s} (d_{hkl}^2 \beta_{hkl} \cos \theta_{hkl}) + \left( \frac{\epsilon_a}{2} \right)^2 \quad (16)$$

where,  $d_{hkl}$  is the lattice spacing,  $V_s$  is the apparent volume weighted average size, and  $\epsilon_a$  is the apparent strain. The apparent strain can be related to root-mean square strain  $\epsilon_{RMS}$  by using the Eq. (17).

$$\langle \epsilon_{RMS} \rangle = \left( \frac{\epsilon_a}{2\sqrt{2\pi}} \right) \quad (17)$$

Figure 5 shows the SSP plot. If  $(d_{hkl}^2 \beta_{hkl} \cos \theta)$  is taken along X-axis and  $(d_{hkl} \beta_{hkl} \cos \theta)^2$  along Y-axis, then the averaged crystallite size can be obtained from the slope of the linear fit. Figure 6 shows the plot between  $\epsilon_{RMS}$  and  $\epsilon_{hkl}$ . From this plot, the  $\epsilon_{RMS}$  value can be obtained.

Table 2 Geometric parameters of ZnO nanoparticles calcined at 500 °C

Scherrer method	Williamson–Hall (W–H) method				Size-strain plot (SSP)			
	$\epsilon \cdot 10^{-3}$	UDM	USDM	UEDEM	$D_v$ (nm)	$\epsilon_a \cdot 10^{-3}$	$\sigma$ (MPa)	$\epsilon_{RMS} \cdot 10^{-3}$
D (nm)	0.951	46.8	46.9	46.8	116.16	1.668	199.24	0.5154
		$\epsilon \cdot 10^{-3}$	$\epsilon \cdot 10^{-3}$	$\epsilon \cdot 10^{-3}$				
		80.61	80.61	111.44				
		0.6748	0.6748	0.933				
		46.8	46.8	52				

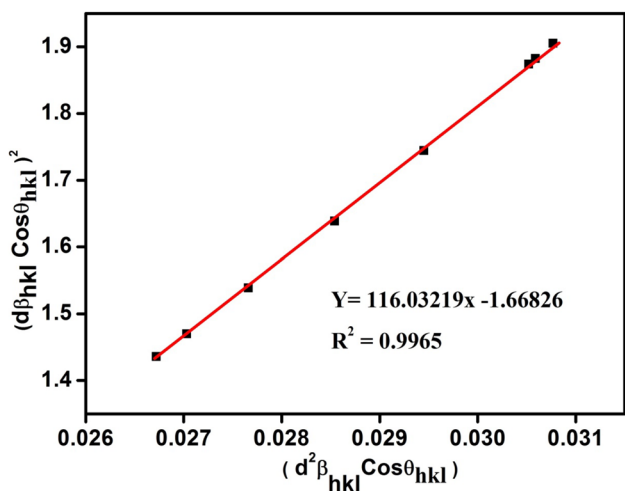


Fig. 5 Plot for  $(d^2_{hkl}\beta_{hkl}\cos\theta)^2$  versus  $(d_{hkl}\beta_{hkl}\cos\theta)^2$

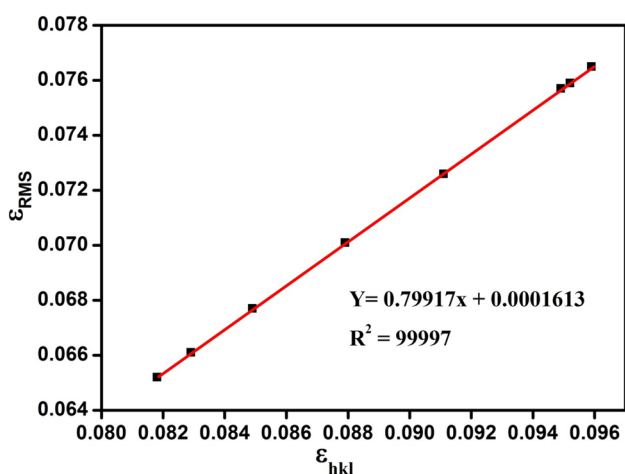


Fig. 6 Plot for  $\epsilon_{RMS}$  versus  $\epsilon_{hkl}$

### 3.3 FTIR spectroscopy

FTIR is an effective characterization technique to confirm the absorption of surfactant molecule at the ZnO surface and the characteristic behaviour of oxides. The FTIR spectra of ZnO nanostructure was obtained in the range of 400–4000  $\text{cm}^{-1}$ . The oxides give absorption bands in the fingerprint region. Figure 7 shows the FTIR spectrum of ZnO nanoparticles. The significant band at 458  $\text{cm}^{-1}$  is the characteristic absorption band of Zn–O stretching mode and the peak at 3405  $\text{cm}^{-1}$  is due to O–H stretching which reveals the presence of small amount of water in

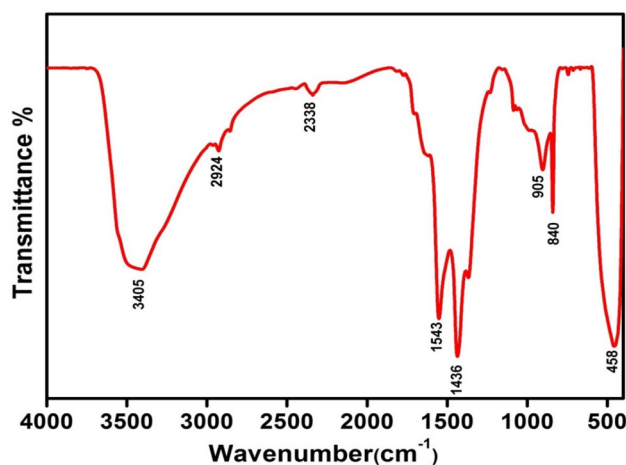


Fig. 7 FTIR spectrum of ZnO nanoflakes

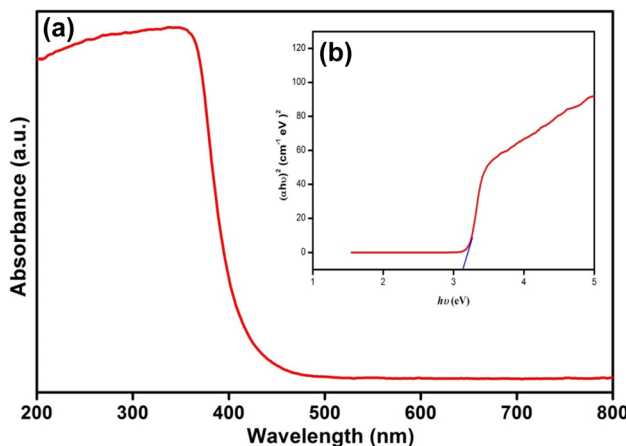


Fig. 8 UV–visible spectrum of ZnO nanoparticles. **a** Absorption spectrum and **b** Tauc plot

the ZnO nanostructure. The obtained data are identical with the previously reported results [11, 16]. The band located at 2338  $\text{cm}^{-1}$  is due to the atmospheric  $\text{CO}_2$  present in the instrument and the band located at 2924  $\text{cm}^{-1}$  is attributed to the C–H stretching vibration. The bands around 1436 and 1543  $\text{cm}^{-1}$  are related to symmetric C=O and C–O stretching vibrations [17].

### 3.4 UV–visible spectroscopy

Figure 8 shows the absorption spectrum of ZnO nanoparticles. The absorption peak was observed at 365 nm from which the band gap was calculated using Tauc plot [11]. The optical band gap of ZnO nanoparticles were calculated from absorption peaks by using Tauc relation [18, 19] which is a plot between  $h\nu$  (eV) versus  $(\alpha h\nu)^2$  ( $\text{cm}^{-1} \text{eV}$ )<sup>2</sup>.



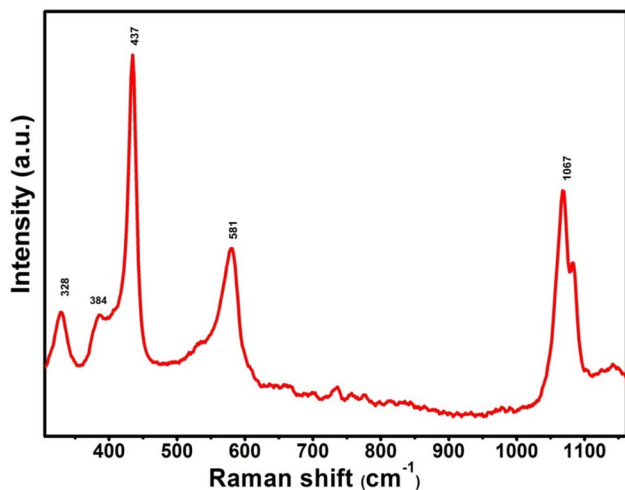


Fig. 9 Raman spectra of ZnO nanoflakes

$$(\alpha h\nu) = C(h\nu - E_g)^n$$

where  $\alpha$  is the absorption coefficient,  $h\nu$  is the energy of incident photons, and  $n$  depends on the type of transition. The transition values: direct band (1/2), indirect band (2), forbidden direct band (3/2) and forbidden indirect band (3). The band gap was determined from the intercept of linear portion of the  $h\nu$  vs  $(\alpha h\nu)^2$  plot. The estimated band gap value is 3.1 eV. The obtained value is lower than the actual experimental band gap value. This is due to the effect of annealing temperature. The optical band gap decreases as temperature and doping concentration increases [4, 20].

### 3.5 Raman spectroscopy

The Raman spectrum is shown in Fig. 9. The ZnO has wurtzite hexagonal structure, which belongs to the space group  $C_{60}^4$  (P63mc) with two formula units per primitive cell and atoms occupying  $C_{3v}$ . The Raman active zone centered optical phonons predicted by group theory are  $A_1 + 2E_2 + E_1$ . The phonons having  $A_1$  and  $E_1$  symmetry are polar phonons and exhibit different frequencies for the transverse optical (TO) and longitudinal optical (LO) phonons. The peaks are obtained at 328, 384, 437, 581, and 1067  $\text{cm}^{-1}$ . The peak at 328  $\text{cm}^{-1}$  is the Raman band which can be assigned to acoustic mode. The peaks at 384 and 581  $\text{cm}^{-1}$  are overtones of  $A_1$  and  $E_1$  symmetry species of transverse optical and longitudinal optical phonon modes, respectively [21, 22]. The peak at 437  $\text{cm}^{-1}$  corresponds to  $E_2$  mode. It is the characteristic band of wurtzite hexagonal phase of ZnO. The peak at 1067  $\text{cm}^{-1}$  is assigned to  $A_1$  and  $E_1$  combination Raman band. The high intensity peak may due to the particle

**Table 3** Wavenumber ( $\text{cm}^{-1}$ ) and symmetry modes of ZnO nanoparticle from Raman spectrum

Wavenumber ( $\text{cm}^{-1}$ )	Symmetry	Process	References [21, 22]
328	$A_1$	Acoustic overtone	331
384	$A_1$ (TO)	First process	383
437	$E_2$	First process	438
581	$E_1$ (LO)	First process	584
1067	$A_1, E_1$	Optical overtone	1154

size which is comparatively bigger. The intensity and particle size are relatively dependent on the Raman band shift which may be due to phonon dispersion in the nanostructure. The particle size and intensity decrease as the Raman band shifts towards the higher wavenumber [23]. In this study, the high intensity band is obtained at 437  $\text{cm}^{-1}$  in the low wave number region, which indicates that the particle size is bigger in the nanostructure which is also confirmed by FE-SEM results. The symmetry modes are given in Table 3.

### 3.6 Field emission scanning electron microscopy (FESEM)

Figure 10 shows the FE-SEM morphology of sol gel synthesized ZnO nanopowder at different magnifications. The obtained result clearly shows that the prepared ZnO exhibits flaky structure. These ZnO nanocrystalline flakes are flat and irregular in shape as observed in the micrographs obtained at higher magnification. The stoichiometry elements in the sample were analysed by using energy dispersive X-ray spectroscopy. The EDAX spectrum is shown in the Fig. 11, The obtained spectrum confirms the presence of Zinc (46.27%) and Oxygen (53.73%) elements in the prepared sample. This result clearly shows that the prepared ZnO nanostructure is highly pure.

### 3.7 Impedance analysis

The electrical properties such as dielectric constant, dielectric loss, and ac conductivity were analyzed from impedance spectroscopy. The experiment was conducted using 8 mm diameter pellets, which were obtained by applying a pressure of 5 tons  $\text{cm}^{-2}$ . Figure 12a–h shows the plots of various parameters against frequency such as dielectric response, dielectric loss, electric modulus, and ac conductivity. The Nyquist plot show in Fig. 12a reveals that the lower frequency dispersion is due to the grain boundary and the higher frequency dispersion due to the grain interior. The dielectric response of ZnO is shown in Fig. 12b and c. The real and imaginary part of the complex permittivity were plotted against frequency, which clearly shows that

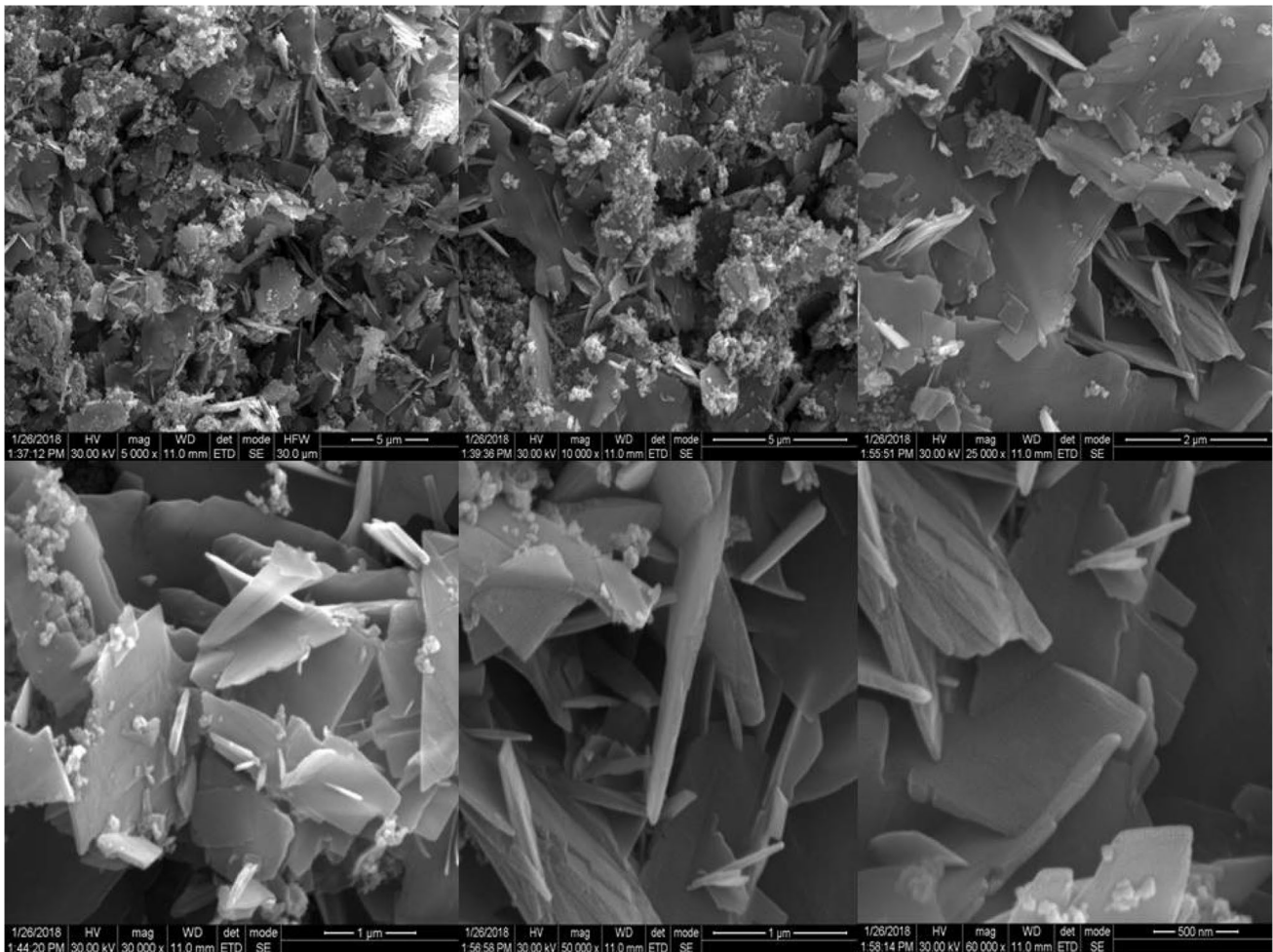


Fig. 10 FE-SEM morphology of ZnO nanoflakes

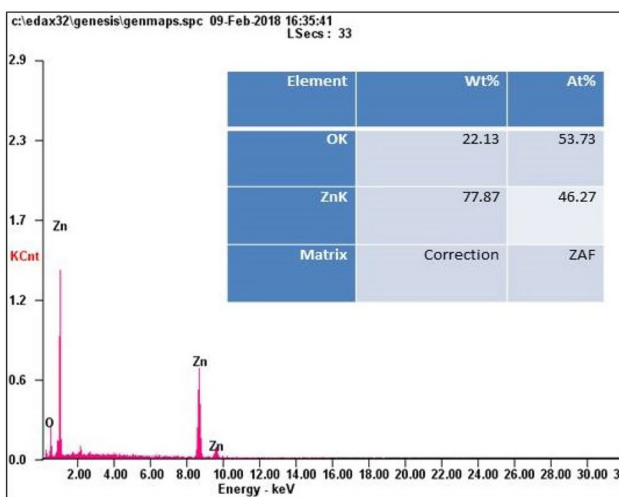


Fig. 11 EDAX spectrum of ZnO nanoflakes

both  $\epsilon'$  and  $\epsilon''$  increase with decreasing frequency and this dielectric behaviour is based on polarization effect present in the ZnO nanostructure [24, 25]. The dielectric response in the low frequency region is due to the existence of space charge polarization. The source of this polarization is grain boundaries and structural inhomogeneity which were confirmed from FE-SEM study [26, 27]. The Fig. 12d and e shows the electric modulus plot in which  $M'$  and  $M''$  gives the real and imaginary dielectric modulus, whereas the real modulus spectra non-linearly increase with increasing frequency. The imaginary modulus plot shows a single relaxation peak in the intermediate frequency region. Figure 12f shows the plot of dielectric loss with frequency. Dielectric loss gives the dissipated energy in the dielectric medium which is due to the domain wall resonance. The obtained result indicates that the dielectric loss increases in frequency. The ac conductivity plot is shown in Fig. 12g and h which can be calculated from the following Eq. (18).

$$\sigma_{ac} = \epsilon' \epsilon_0 \omega \tan \delta \quad (18)$$



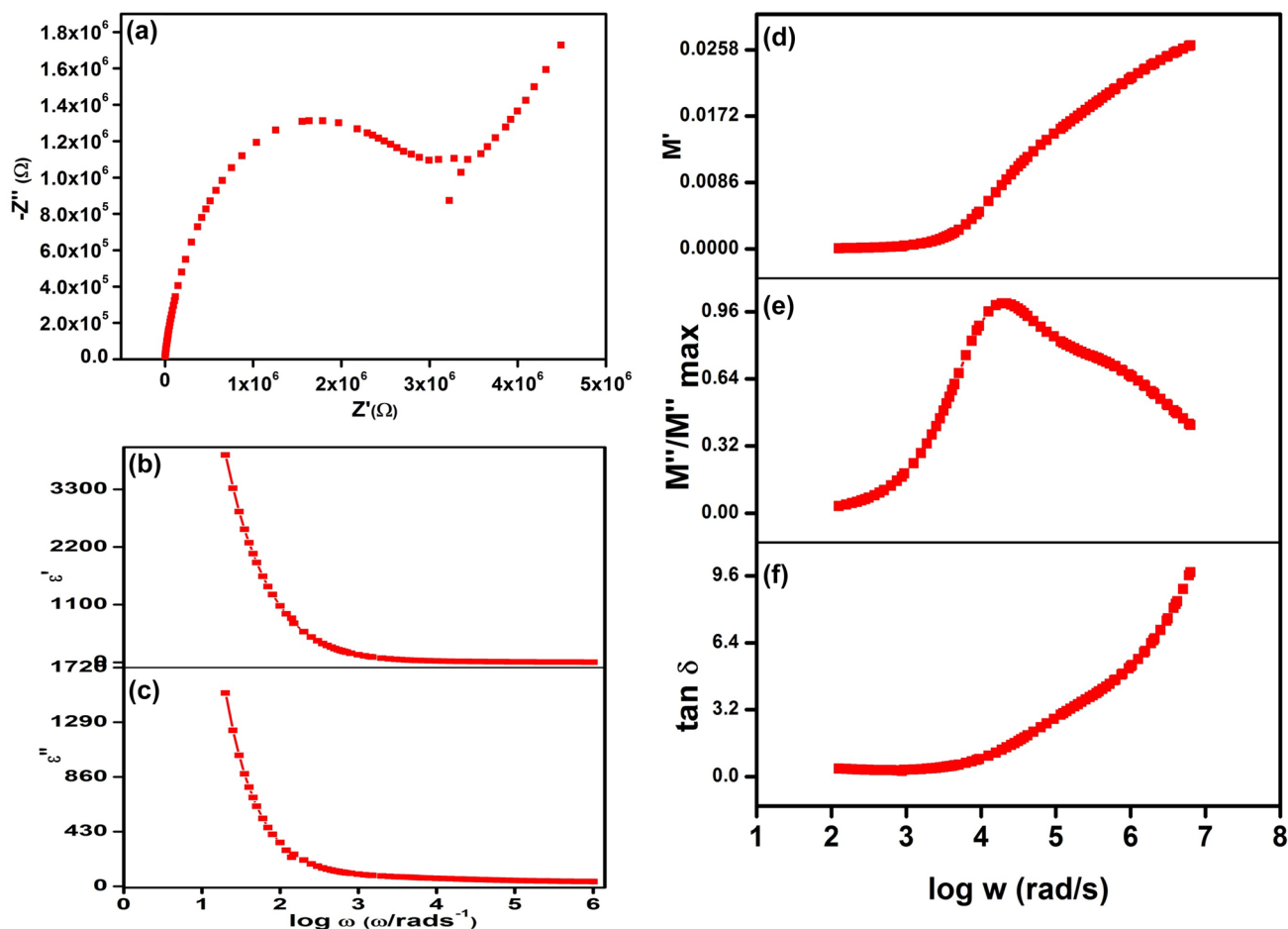


Fig. 12 a–h Impedance analysis of ZnO nanoflakes

where,  $\omega$  is the angular frequency,  $\epsilon'$  is dielectric constant,  $\epsilon_0$  is permittivity of free space ( $8.854 \times 10^{-12}$ ), and  $\tan\delta$  gives the dielectric loss.

The obtained conductivity plot shows the frequency dependent behaviour [24, 28]. At high frequency, the ac conductivity is also high but at low frequency the conductivity becomes almost constant. This behaviour reveals that the ac conductivity is largely dependent on frequency. The empirical formula of frequency dependent ac conductivity is given in Eq. (19).

$$\sigma_{ac}(\omega) = B\omega^n \quad (19)$$

where,  $n$  is a dimensionless constant, which has the value between 0 and 1, if  $n=0$ , the conductivity is independent of frequency and is called dc conductivity. If  $n \leq 1$ , then the conductivity becomes frequency dependent, that is the ac conductivity. The value 'n' can be obtained from the slope of  $\ln \sigma_{ac}$  plot against frequency, which is shown in Fig. 12h. The obtained value of  $n$  is 0.7264, and it confirms that the material exhibits ac conductivity.

### 3.8 Photocatalytic activity

Photocatalytic study was carried out on methylene blue dye (MB) with ZnO nanoparticles by using UV light illumination. Methylene blue is a generally referred organic dye for photo degradation study, which is a hazardous dye as it causes many biological and environmental problems [18]. ZnO nanoparticles are promising candidates for degradation of methylene blue due to its higher efficiency of generation and mobility of photo induced electrons and holes. Electrons and holes are created when the photocatalyst is irradiated with UV light. These generated electrons affect the conjugation of dyes and decompose. The holes generated, creates the  $\text{OH}^-$  from water which degrades the dye. The process is given in the following schematic diagram (Fig. 13) and equations.



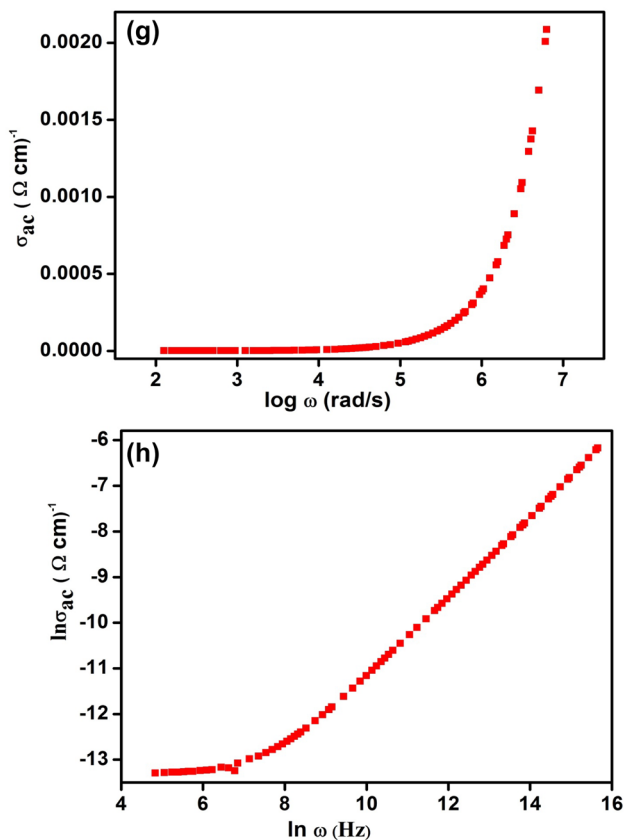
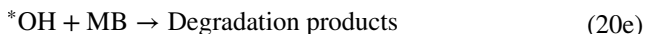
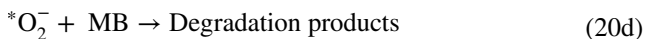


Fig. 12 (continued)



The effectiveness of ZnO nanoparticles to degrade methylene blue dye was studied with varying irradiation time [18, 29]. The degradation efficiency was calculated using Eq. (21).

$$\text{Photodegradation (\%)} = \left[ \frac{C_t - C_0}{C_0} \right] \times 100 \quad (21)$$

where,  $C_0$  is the initial concentration,  $C_t$  is the residue concentration after time ‘t’ of photodegradation.

The obtained results are shown in Fig. 14a–c. Figure 14a represents the behaviour of the dye concentration with respect to time. It shows that the whole photo degradation process is completed within 180 min. Figure 14b shows the rate of degradation of methylene blue with time. The results clearly show that 80% degradation is completed within 60 min. 95% degrades at 180 min. This result indicates that the ZnO nanoparticles synthesized in the present work is a suitable photocatalyst for the degradation of methylene blue dye (MB). The percentage of degradation with respect to time is presented in Table 4. The kinetics and rate constant were calculated using Langmuir–Hinshelwood mechanism, which is given by the following Eq. (22).

$$r = \frac{-dc}{dt} = \frac{kKC}{1 + KC} \quad (22)$$

where,  $r$  is the degradation rate of the reactant (mg/l min),  $C$  is the concentration of the reactant (mg/l),  $t$  is the irradiation time,  $k$  is the reaction rate constant (mg/l min), and  $K$  is the adsorption constant of the reactant (l/mg). When  $C$  is very small, the equation can be modified as follows.

$$\ln\left(\frac{C_0}{C_t}\right) = kKt = K_{app}t \quad (23)$$

where  $K_{app}$  is the apparent first-order rate constant, which is given by the slope of the graph of  $\ln\left(\frac{C_0}{C_t}\right)$  versus time plot [30, 31]. Figure 14c shows the linear relationship between  $\ln(C_0/C_t)$  and irradiation time. The result clearly indicates that photodegradation of methylene blue (MB) follows first order kinetics and the rate constant was calculated as  $0.0296 \text{ min}^{-1}$ . The results obtained in this study, provided in Table 5 are in good agreement with the earlier reports [29,

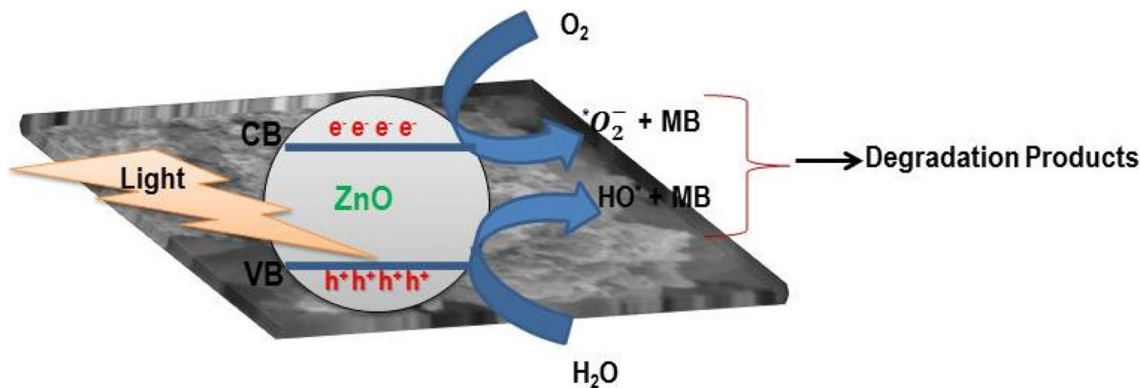
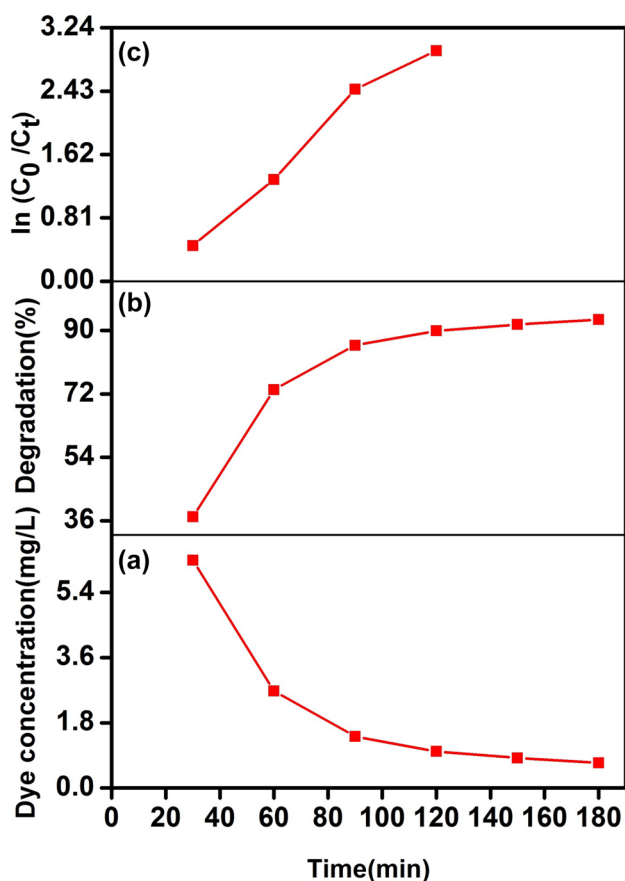


Fig. 13 Schematic representations of photocatalytic degradation mechanism in MB dye in the presence of ZnO catalyst



**Fig. 14** a–c Photocatalytic activity of MB with ZnO nanoflakes. **a** Dye concentration with time. **b** Dye degradation with time. **c**  $\ln(C_0/C_t)$  versus time

**Table 4** Degradation percentage and  $\ln(C_0/C_t)$  values of Methylene blue (MB) dye with ZnO nanoflakes

Time (min)	% Degradation	$\ln(C_0/C_t)$
30	37.1	0.4636
60	73.2	1.3168
90	85.8	1.9519
120	89.9	2.2926
150	91.7	2.4889
180	93.6	2.6736

**Table 5** Comparison table for the rate constant ( $K_{app}$ ) of the photocatalytic degradation with ZnO as catalyst

Morphology	Rate constant ( $K_{app}$ ) ( $\text{min}^{-1}$ )	References
Spherical	$1.29 \times 10^{-2}$	[29]
Hexagon	$2 \times 10^{-4}$	[32]
Flower-like nanorod	$7 \times 10^{-4}$	[33]
Micro needle	$1.1 \times 10^{-3}$	[33]
Flower like structure	$3.5 \times 10^{-3}$	[33]
Nanoflake	$2.96 \times 10^{-2}$	Present work

[32, 33]. It also confirms the enhanced photocatalytic behaviour of ZnO nanoparticles for MB dye degradation.

## 4 Conclusion

In this work, ZnO nanoparticles were synthesized by the sol–gel method and various characterizations such as, XRD, FE-SEM, UV–Vis, Raman, FTIR, Impedance, and Photocatalysis studies were done. The wurtzite hexagonal ZnO structure was confirmed from XRD and the calculated crystallite size is 21.84 nm. Also, the structural and geometric parameters such as, crystallite structure, lattice parameter, strain, stress, and energy density were obtained using Scherrer and Williamson–Hall models. The UV–Vis study gives the absorption wavelength and band gap. The characteristic peaks of ZnO nanoparticles are obtained at 437 and 458  $\text{cm}^{-1}$  respectively from Raman and FTIR analysis. The electrical properties were analysed using Impedance spectroscopy. The dielectric studies reveal that the dielectric constant is higher at low frequency and decreases while moving towards higher frequency. The dielectric loss and the ac conductivity increased with frequency. Photocatalytic studies on the prepared ZnO nanoflakes demonstrate the enhanced photodegradation of methylene blue dye.

**Acknowledgements** The author B. Manikandan thank University Grants Commission, India for the financial support through UGC-RGNFD (University Grants Commission-Rajiv Gandhi National Fellowship for student with Disabilities) - Award letter No: F./2013-14/RGNF-2013-14D-OBC-TAM-56670; Dt: 30-10-2013).

## References

1. C. Tian, Q. Zhang, A. Wu, M. Jiang, Z. Liang, B. Jiang, H. Fu, Chem. Commun. **48**, 2858–2860 (2012)
2. J. Ungula, B.F. Dejene, Physica B **480**, 26–30 (2016)
3. H.R. Ghorbani, Orient. J. Chem. **31**(2), 1219–1221 (2015)
4. S.S. Kumar, P. Venkateswarlu, V.R. Rao, G.N. Rao, Int. Nano Lett. **3**, 30 (2013)
5. S.S. Kulkarni, M.D. Shirsat, Int. J. Adv. Res. Phys. Sci. **2**, 14–18 (2015)
6. G. Amin, M.H. Asif, A. Zainelabdin, S. Zaman, O. Nur, M. Willander, J. Nanomater. **2011**, 5 (2011)
7. A. Vanaja, G.V. Ramaraju, K.S. Rao, Int. J. Techno Chem. Res. **2**(2), 110–120 (2016)
8. K. Swaroop, H.M. Somashekarappa, Res. J. Recent Sci. **4**(ISC-2014), 197–201 (2015)
9. K.G. Chandrappa, T.V. Venkatesha, Nano-Micro Lett. **4**(1), 14–24 (2012)
10. Y.T. Prabhu, K.V. Rao, V.S.S. Kumar, B.S. Kumari, World J. Nano Sci. Eng. **4**, 21–28 (2014)
11. A. Vanaja, G.V. Ramaraju, K.S. Rao, Indian J. Sci. Technol. **9**(12), 87013 (2016)
12. S. Anitha, S. Muthukumar, J. Mater. Sci. **28**, 12995–13005 (2017)

13. A.K. Kalita, S. Karmakar, *Int. J. Innov. Res. Sci. Eng. Technol.* **6**, 4 (2017)
14. P. Bindu, S. Thomas, *J. Theoret. Appl. Phys.* **8**, 123–134 (2014)
15. N. Abraham, A. Rufus, C. Unni, D. Philip, *J. Mater. Sci.* **28**, 16527–16539 (2017)
16. H. Kumar, R. Rani, *Int. Lett. Chem. Phys. Astron* **14**, 26–36 (2013)
17. S.S. Alias, A.B. Ismail, A.A. Mohamad, *J. Alloys Compd.* **499**, 231–237 (2010)
18. S. Kant, A. Kumar, *Adv. Mater. Lett.* **3**(4), 350–354 (2012)
19. N. Akcay, G. Algun, N.U. Kılıc, S. Shawuti, M.M. Can, *J. Mater. Sci.* **28**, 4492–4497 (2017)
20. K. Omri, I. Najeh, R. Dhahri, J. El Ghoul, L. El Mir, *Microelectron. Eng.* **128**, 53–58 (2014)
21. A.K. Ojha, M. Srivastava, S. Kumar, R. Hassanein, J. Singh, M.K. Singh, A. Materny, *Vib. Spectrosc.* **72**, 90–96 (2014)
22. R.P. Wang, G. Xu, P. Jin, *Phys. Rev. B* **69**, 113303 (2004)
23. H.C. Choi, Y.M. Jung, S.B. Kim, *Vib. Spectrosc.* **37**, 33–38 (2005)
24. M. Mujahid, *Bull. Mater. Sci.* **38**, 995–1001 (2015)
25. N. Kılınc, L. Arda, S. Öztürk, Z.Z. Öztürk, *Cryst. Res. Technol.* **45**, 529–538 (2010)
26. Y. Cherifi, A. Chaouchi, Y. Lorgoilloux, M. Rguiti, A. Kadri, C. Courtois, *Process. Appl. Ceram.* **10**(3), 125–135 (2016)
27. S. Choudhary, R.J. Sengwa, *Adv. Mater. Proc.* **2**(5), 315–324 (2017)
28. M.M. Hassan, A.S. Ahmed, M. Chaman, W. Khan, A.H. Naqvi, A. Azam, *Mater. Res. Bull.* **47**, 3952–3958 (2012)
29. A.B. Lavand, Y.S. Malghe, *J. Asian Ceram. Soc.* **3**, 305–310 (2015)
30. H.S. Aliyu, A.H. Abdullah, Z. Abbas, *Int. J. Multi. Res. Dev.* **2**(3), 612–615 (2015)
31. S.S.M. Hassan, W.I.M. El Azab, H.R. Ali, M.S.M. Mansour, *Adv. Nat. Sci.* **6**, 045012 (2015)
32. K.P. Raj, K. Sadaiyandi, A. Kennedy, S. Sagadevan, *J. Mater. Sci.* (2017). <https://doi.org/10.1007/s10854-017-7857-7>
33. A. Phuruangrat, O. Yayapao, S. Thongtem, T. Thongtem, *Russ. J. Phys. Chem. A* **90**(5), 949–954 (2016)